JACS
JOURNAL OF THE AMERICAN CHEMICAL SOCIETY
pubs.acs.org/JACS
Article

Multimodal Structure Solution with ^{19}F NMR Crystallography of Spin Singlet Molybdenum Oxyfluorides

Fenghua Ding,[⊥] Kent J. Griffith,[⊥] Can P. Koçer, Richard J. Saballos, Yiran Wang, Chi Zhang, Matthew L. Nisbet, Andrew J. Morris,* James M. Rondinelli,* and Kenneth R. Poeppelmeier*

Cite This: *J. Am. Chem. Soc.* 2020, 142, 12288−12298
Read Online

ABSTRACT: Complex crystal structures with subtle atomic-scale details are now routinely solved using complementary tools such as X-ray and/or neutron scattering combined with electron diffraction and imaging. Identifying unambiguous atomic models for oxyfluorides, needed for materials design and structure−property control, is often still a considerable challenge despite their advantageous optical responses and applications in energy storage systems. In this work, NMR crystallography and single-crystal X-ray diffraction are combined for the complete structure solution of three new compounds featuring a rare triangular early transition metal oxyfluoride cluster, $[Mo_3O_4F_9]^{5-}$. After framework identification by single-crystal X-ray diffraction, 1D and 2D solid-state ^{19}F NMR spectroscopy supported by *ab initio* calculations are used to solve the structures of $K_5[Mo_3O_4F_9]\cdot 3H_2O$ (**1**), $K_5[Mo_3O_4F_9]\cdot 2H_2O$ (**2**), and $K_{16}[Mo_3O_4F_9]_2[TiF_6]_3\cdot 2H_2O$ (**3**) and to assign the nine distinct fluorine sites in the oxyfluoride clusters. Furthermore, ^{19}F NMR identifies selective fluorine dynamics in $K_{16}[Mo_3O_4F_9]_2[TiF_6]_3\cdot 2H_2O$. These dual scattering and spectroscopy methods are used to demonstrate the generality and sensitivity of ^{19}F shielding to small changes in bond length, on the order of 0.01 Å or less, even in the presence of hydrogen bonding, metal−metal bonding, and electrostatic interactions. Starting from the structure models, the nature of chemical bonding in the molybdates is explained by molecular orbital theory and electronic structure calculations. The average Mo−Mo distance of 2.505 Å and diamagnetism in **1**, **2**, and **3** are attributed to a metal−metal bond order of unity along with a $1a^2 1e^4$ electronic ground state configuration for the $[Mo_3O_4F_9]^{5-}$ cluster, leading to a rare trimeric spin singlet involving d^2 Mo^{4+} ions. The approach to structure solution and bonding analysis is a powerful strategy for understanding the structures and chemical properties of complex fluorides and oxyfluorides.

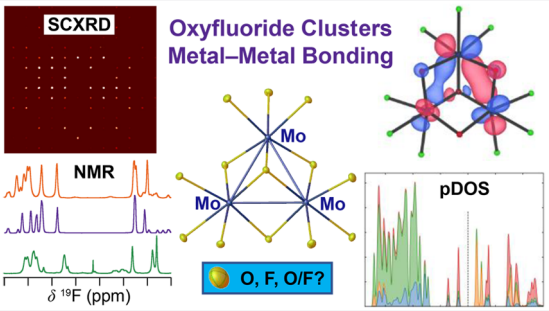

■ INTRODUCTION

Heteroanionic compounds,[1,2] particularly oxyfluorides, garner wide interest as nonlinear optical materials[3−6] and next-generation rechargeable battery cathodes.[7−9] Structures with metal−metal bonds, especially those of molybdenum, are of importance in catalysis chemistry,[10,11] single-component magnetic conductors,[12] multimetal-cluster metal−organic frameworks (MOFs), dielectric materials,[13] and multivalent rechargeable batteries (e.g., Mo_6S_8).[14−17] Compounds incorporating such functional motifs, individually or in combination, comprise a large and promising space for future materials discovery but are challenging to fully characterize. For example, differentiating oxygen and fluorine remains a serious challenge due to the limited scattering contrast between this pair by X-rays, neutrons, or electrons. In favorable cases with ordered anions, bond valence analysis can sometimes be used for indirect assignment. On the other hand, solid-state NMR spectroscopy serves as a direct probe of the local environment, bonding, and dynamics. Fluorine NMR is aided by favorable nuclear and electronic properties such as the 100% natural abundance and the high gyromagnetic ratio of ^{19}F, and a chemical shift range spanning 800 ppm. In this work, we explored the molybdenum oxyfluoride phase space with hydrosolvothermal HF synthesis methods and then exploited the combination of NMR and X-ray crystallography to achieve full structure solutions of three new compounds featuring Mo−Mo bonds, an ordered heteroanion array, and, in one case, fluorine dynamics.

Molybdenum is known to form metal−metal bonds from solution because the early 4d and 5d metals in their lower oxidation states have virtually no aqua complexes (e.g., $[Mo(H_2O)_6]^{4+}$ ions) and instead readily form isolated trinuclear clusters. These clusters are known to form metal−metal-bonded triangular core structures $[M_3L_{13}]$ consisting of three octahedra fused together so that each octahedron shares

Received: April 13, 2020
Published: June 12, 2020

https://dx.doi.org/10.1021/jacs.0c04019
J. Am. Chem. Soc. 2020, 142, 12288−12298

one vertex and two edges (Figure 1). The structure has a three-coordinate capping apical ligand above (position X) and three

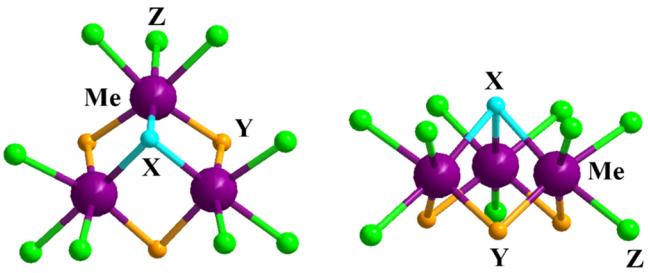

Figure 1. Structure of $[M_3L_{13}]$ formulated as $(MX_{1/3}Y_{2/2}Z_3)_3$.

bridging ligands below (position Y) the plane occupied by the metals. Nine more terminal ligands (position Z) complete the cluster. Among the Z ligands, three are coplanar with the Y ligands and the other six surround the apical X ligand on the other side of the plane formed by the metal atoms. The different electron shielding environment of these two types of Z sites enables them to host different ligands. Ligand substitutability makes the cluster structure $[M_3L_{13}]$ a versatile prototype with multiple local environments that are well-suited for heteroanionic materials design.[18]

In previous studies of this class of compounds, series of oxo, sulfido, selenido, mixed oxo-sulfido, and chalcogenido complexes of molybdenum have been reported,[10,19,20] with chalcogenide cluster compounds being the most studied. In the case of oxo-molybdenum clusters, the Mo_3O_{13} unit has been widely pursued to explore complex magnetic phases because its 2D $[Mo_3O_8]$ layer hosts a spin 1/2 Mo_3 cluster (e.g., $Li_2ScMo_3O_8$ and $Li_2ZnMo_3O_8$).[21−23] Isolated trinuclear oxo clusters with the $[Mo_3O_4]^{4+}$ moiety and a variety of anionic ligands have also been examined.[24−27] However, only a limited number of molybdenum oxyfluoride clusters have been proposed,[28,29] and O/F ordering and bridging oxygen are not taken for granted in Mo clusters.[30,31]

In the present work, we report the structures of three compounds, $K_5[Mo_3O_4F_9]\cdot 3H_2O$, $K_5[Mo_3O_4F_9]\cdot 2H_2O$, and $K_{16}[Mo_3O_4F_9]_2[TiF_6]_3\cdot 2H_2O$, which contain the $[Mo_3O_4F_9]^{5-}$ cluster. We demonstrate the application of complementary single-crystal X-ray diffraction, ^{19}F solid-state NMR spectroscopy, and *ab initio* calculations to obtain a complete structure solution including the identification of oxygen and fluorine positions within the $[Mo_3O_4F_9]^{5-}$ cluster. 1D ^{19}F NMR provides insights into the number of inequivalent fluorine sites, and 2D $^{19}F-^{19}F$ spin exchange experiments can identify spatial relationships between fluorine signals. Spin-exchange is a through-space measurement, wherein magnetization is transferred between nuclei via the r^3-dependent dipolar coupling mechanism where r is the internuclear distance. In addition, nuclear relaxation times of the nuclei provide insight into the electronic structure and dynamics of a material, which are difficult to obtain with other methods. As a result, NMR crystallography[32] methods yield detailed information that is used to select and validate precise structure models for the three $[Mo_3O_4F_9]^{5-}$ complexes. Fluorine is found to occupy all Z positions, while oxygen sits on the X and Y sites. There is no evidence for static or dynamic fluoride disorder within the cluster; however, fluorine motion is identified in isolated $[TiF_6]^{2-}$ polyhedra. Magnetic measurements and optical characterization via Raman and infrared spectroscopy and electron and phonon density-of-states calculations provide additional structural details and allow us to assign the $1a^21e^4$ ground-state electronic configuration as a $S = 0$ spin singlet

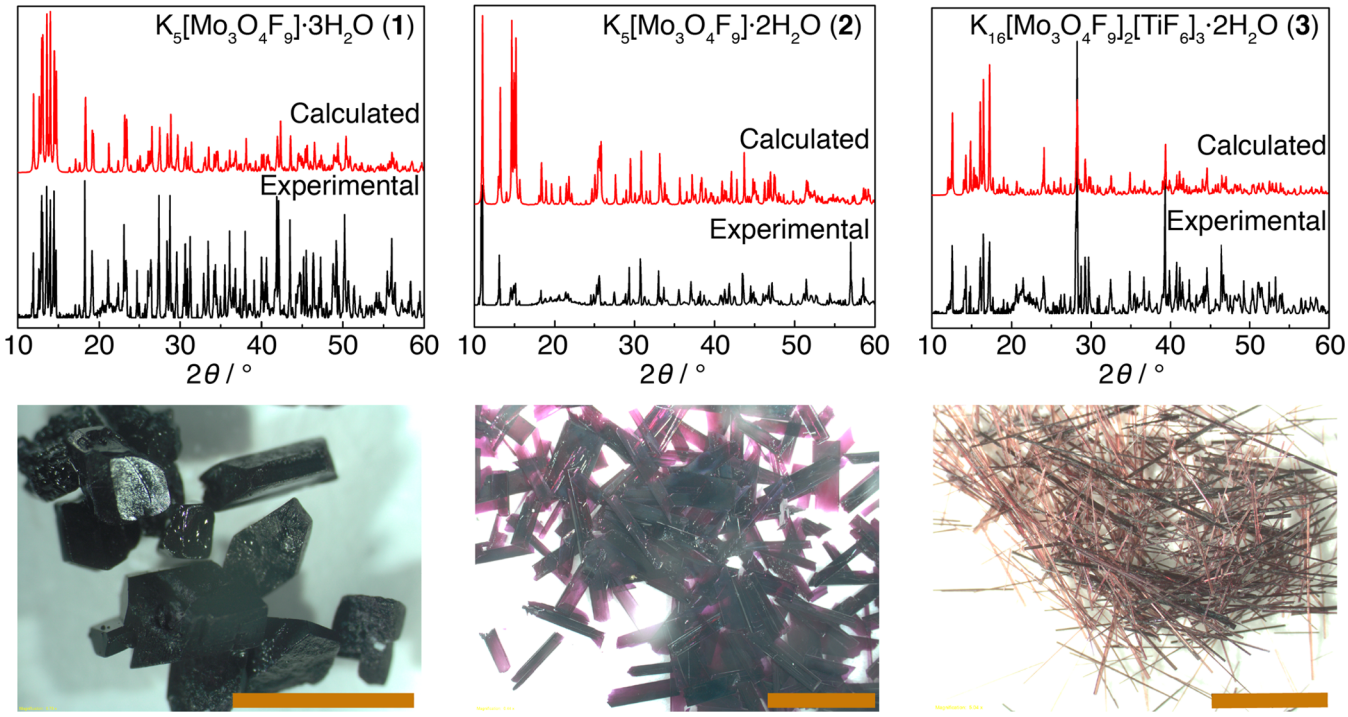

Figure 2. Photographs of crystals and X-ray powder diffraction patterns for $K_5[Mo_3O_4F_9]\cdot 3H_2O$, $K_5[Mo_3O_4F_9]\cdot 2H_2O$, and $K_{16}[Mo_3O_4F_9]_2[TiF_6]_3\cdot 2H_2O$. The scale bars in the photographs (at bottom right) are 5 mm in **1** and **2** and 0.5 mm in **3**. Preferred orientation effects are present in the powder patterns.

https://dx.doi.org/10.1021/jacs.0c04019
J. Am. Chem. Soc. 2020, 142, 12288−12298

Table 1. Crystal Data and Structure Refinement of 1, 2, and 3

empirical formula	$K_5[Mo_3O_4F_9]\cdot 3H_2O$ (**1**)	$K_5[Mo_3O_4F_9]\cdot 2H_2O$ (**2**)	$K_{16}[Mo_3O_4F_9]_2[TiF_6]_3\cdot 2H_2O$ (**3**)	$K_{16}[Mo_3O_4F_9]_2[TiF_6]_3\cdot 2H_2O$ (**3**)
CCDC number	1979705	1979704	1979703	1987370
formula weight /g mol^{-1}	772.37	754.35	2192.97	2192.97
temperature/K	100	100	100	296
space group	$P2_1/c$	$P2_1/n$	$P2_1/n$	$P2_1/n$
a/Å	13.121(3)	7.424(4)	6.313(4)	6.337(10)
b/Å	7.928(2)	12.084(5)	24.686(15)	24.865(2)
c/Å	14.928(4)	16.085(8)	14.621(9)	14.713(10)
β/deg	97.4(10)	91.6(2)	94.5(2)	94.4(10)
volume/Å^3	1539.9(7)	1442.73(12)	2271.5(2)	2311.28(4)
Z	4	4	2	2
ρ_{calc}/g cm^{-3}	3.396	3.537	3.244	3.151
μ/mm^{-1}	3.915	4.165	3.764	3.683
F(000)	1460.0	1424.0	2072.0	2060.0
crystal size/mm^3	0.204 × 0.111 × 0.073	0.226 × 0.187 × 0.121	0.197 × 0.147 × 0.102	0.178 × 0.108 × 0.044
radiation	Mo Kα (λ = 0.71073)	Mo Kα (λ = 0.71073)	Mo Kα (λ = 0.71073)	Mo Kα (λ = 0.71073)
2θ range for data collection/deg	9.732 to 79.526	4.216 to 85.284	3.246 to 74.488	4.294 to 67.708
index ranges	$-23 \le h \le 23$, $-14 \le k \le 14$, $-22 \le l \le 26$	$-13 \le h \le 14$, $-22 \le k \le 22$, $-30 \le l \le 29$	$-5 \le h \le 10$, $-42 \le k \le 42$, $-24 \le l \le 24$	$-9 \le h \le 9$, $-38 \le k \le 38$, $-22 \le l \le 21$
data/restraints/parameters	9207/0/218	10081/0/209	11717/0/322	8617/0/331
goodness of fit on F^2	1.039	1.037	1.062	1.058
final R indexes [$I \ge 2\sigma(I)$][a]	R_1 = 0.033, wR_2 = 0.074	R_1 = 0.025, wR_2 = 0.064	R_1 = 0.025, wR_2 = 0.064	R_1 = 0.018, wR_2 = 0.041
largest diff. peak/hole /e Å^{-3}	1.05/−1.46	1.20/−2.00	2.64/−2.91	0.93/−1.17

[a] $R_1 = \sum||F_0| - |F_c||/\sum|F_0|$ and $wR_2 = [\sum w(F_0^2 - F_c^2)^2/\sum wF_o^4]^{1/2}$ for $F_0^2 > 2\sigma(F_0^2)$.

arising from Mo−Mo metal bonding within the Mo_3 triangular unit within the $[Mo_3O_4F_9]^{5-}$ cluster.

■ EXPERIMENTAL PROCEDURES

Caution! *Hydrofluoric acid is toxic and corrosive. It must be handled with extreme caution and the appropriate protective equipment and training.*

Reagents. Potassium fluoride (KF, 99.0%), dipotassium titanium hexafluoride (K_2TiF_6, 99.0%), methanol (CH_3OH), and hydrofluoric acid (48.0% HF(aq) by weight) were used as received from Sigma-Aldrich. Deionized (DI) water was used in the synthesis.

Preparation of $K_5[Mo_3O_4F_9]\cdot 3H_2O$. $K_5[Mo_3O_4F_9]\cdot 3H_2O$ (**1**) was synthesized by the reaction of 0.025 mol of MoO_3 (3.600 g), 0.15 mol of KF (8.700 g), and 10 μL of hydrofluoric acid through a hydrosolvothermal method in a 125 mL Teflon-lined Parr pressure vessel filled with 9 mL of deionized H_2O and 9 mL of methanol as backfill. Pressure vessels were heated to 250 °C for 72 h, followed by cooling to room temperature at a rate of 0.1 °C/min. The Teflon-lined Parr autoclave was then left undisturbed at room temperature for another 48 h to allow crystallization. Crystals of $K_5[Mo_3O_4F_9]\cdot 3H_2O$ were finally recovered with a yield of about 15% based on Mo via vacuum filtration and vacuum drying (Figure 2).

Preparation of $K_5[Mo_3O_4F_9]\cdot 2H_2O$. $K_5[Mo_3O_4F_9]\cdot 2H_2O$ (**2**) was synthesized with the same reagents and procedures as for compound **1**, except a larger amount of MoO_3 (0.030 mol, 4.320 g) was used (Figure 2). The yield of **2** is about 20% based on Mo.

Preparation of $K_{16}[Mo_3O_4F_9]_2[TiF_6]_3\cdot 2H_2O$. $K_{16}[Mo_3O_4F_9]_2[TiF_6]_3\cdot 2H_2O$ (**3**) was synthesized by the reaction of 0.01 mol of MoO_3 (1.44 g), 0.01 mol of K_2TiF_6 (2.40 g), and 0.05 mol of KF (2.90 g) through a hydrosolvothermal method within a 125 mL Teflon-lined Parr pressure vessel filled with 20 mL of deionized H_2O and 20 mL of methanol as backfill. The heating and cooling procedures are identical to those used in the preparation of $K_5[Mo_3O_4F_9]\cdot 3H_2O$ (Figure 2). The yield of **3** is about 15% based on Mo.

Powder XRD Diffraction. The PXRD measurements were performed at room temperature on a Rigaku Ultima diffractometer with graphite monochromatized Cu Kα (λ = 1.5418 Å) radiation. The measured powder XRD patterns of ground crystals of **1**, **2**, and **3** were in agreement with the simulated patterns from single-crystal X-ray diffraction studies (Figure 2).

Structure Solution and Refinement Methods. Red, transparent block crystals were chosen for structure determination. Single-crystal XRD data was obtained at 100 K with a Bruker Kappa APEX 2 CCD diffractometer with monochromated Mo Kα radiation (λ = 0.7107 Å). The crystal-to-detector distance was set to 60 mm. The SAINT program was used for data reduction and integration.[32] The structures were established by direct methods and refined through full matrix least-squares fitting on F^2 using OLEX2.[33] All atoms were refined using full matrix least-squares techniques, and final least-squares refinement was on F_0^2 with data $F_0^2 \ge 2\sigma(F_0^2)$. Numerical absorption corrections were carried out using the SADABS program for an area detector. The structure was solved with the use of SHELXS to determine the atomic coordinates of the metallic cations.[34] The structure was examined for possible missing symmetry elements with PLATON, and no additional symmetry was found.[35] The crystal data and structure refinement for $K_5[Mo_3O_4F_9]\cdot 3H_2O$, $K_5[Mo_3O_4F_9]\cdot 2H_2O$, and $K_{16}[Mo_3O_4F_9]_2[TiF_6]_3\cdot 2H_2O$ are summarized in Table 1. Other crystallographic data are reported as CIFs.

Solid-State Nuclear Magnetic Resonance Spectroscopy. NMR spectra were recorded in a static magnetic field of 9.4 T with a Bruker Avance III spectrometer. The samples were packed into 1.6-mm-diameter zirconia rotors, and spectra were recorded at variable magic-angle spinning (MAS) rates of up to 40 kHz in a Phoenix narrow-bore 1.6 mm HFX probe. One-dimensional ^{19}F spectra were measured with a rotor-synchronized Hahn-echo ($\pi/2-\tau-\pi-\tau-$acquire) pulse sequence using a 90° rf pulse of 1.3−1.75 μs and a quantitative recycle delay of $>5T_1$, which proved to be 60 s for **1** and **2** and 3 s for **3**. Variable-temperature MAS spectra of **3** were collected with a center-packed sample. MAS and external

https://dx.doi.org/10.1021/jacs.0c04019
J. Am. Chem. Soc. 2020, 142, 12288−12298

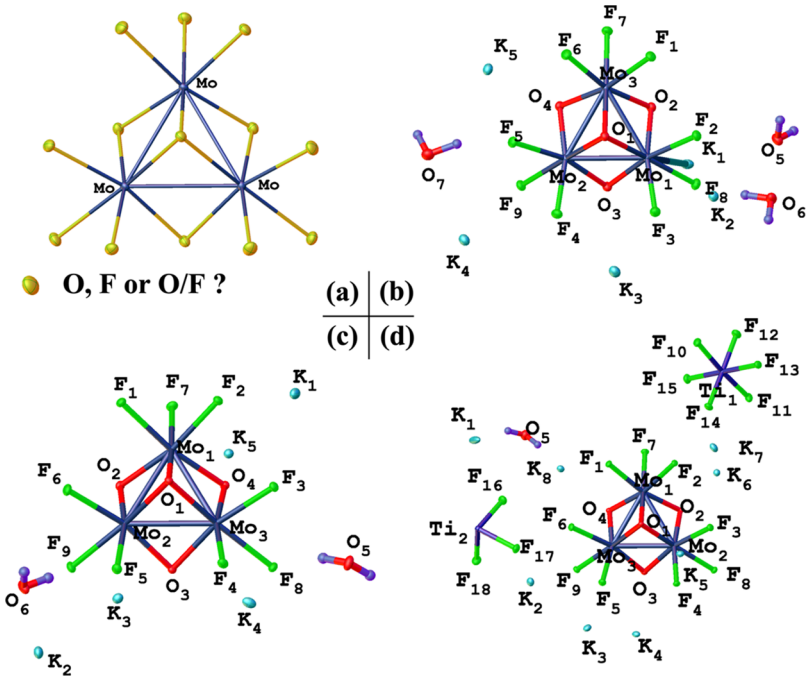

Figure 3. (a) $[Mo_3X_{13}]$ model determined by X-ray diffraction and the proposed asymmetric unit models of (b) **1**, (c) **2**, and (d) **3**. The K−F and K−O bonds are removed for clarity. Atoms are shown as thermal ellipsoids at 50% probability.

heating/cooling affect the sample temperature, which differs from the probe thermocouple, so the actual sample temperature was calibrated via the temperature-dependent shift of lead nitrate.[36,37] Two-dimensional dipolar-coupling-mediated spin-exchange spectra were collected over a range of mixing times (τ_m) with a $\pi/2-t_1-\pi/2-\tau_m-$acquire pulse sequence. For the 2D spectra, a 1 s recycle delay was used, corresponding to about $2T_1$; 16 scans were collected in $F2$, and 1728 points were collected in $F1$ due to the wide range of shifts and T_2* coherence times of up to 1.0 ms. The total measurement time was approximately 8 h for each 2D spectrum. All ^{19}F spectra were externally referenced to the center of the doublet in $NaPF_6$ at −82.5 ppm (40 kHz MAS).

***Ab Initio* Calculations.** Density-functional theory (DFT) calculations were performed with the CASTEP plane wave pseudopotential code.[38] The calculations used the PBE exchange−-correlation functional[39] and Vanderbilt ultrasoft pseudopotentials.[40] The structures were first relaxed using a plane wave energy cutoff of 800 eV, and a Monkhorst−Pack[41] grid with a spacing finer than $2\pi \times 0.04$ Å^{-1} was used to sample the Brillouin zone. Both lattice parameters and atomic positions were optimized until the force on any atom was smaller than 5 meV·Å^{-1}. In addition, for structure **3**, optimizations of the atomic positions were performed in cells for which the lattice parameters were fixed to the experimental values at 100 and 300 K. This was done to mimic the effect of thermal expansion and thus assess the temperature sensitivity of the NMR calculations. Both the chemical shielding tensors and electric field gradient tensors were calculated for the nuclei in all three structures.[42] Calculations of the chemical shielding employed the gauge-including projector augmented wave (GIPAW) method.[43] The NMR calculations used the same plane wave kinetic energy cutoff and Brillouin zone sampling parameters as the geometry optimizations. Density of states calculations were performed with a grid spacing of $2\pi \times 0.02$ Å^{-1}, and the results were postprocessed with the OptaDOS package[44] using a fixed broadening scheme.

Energy-Dispersive X-ray Spectroscopy (EDS). Surface imaging and composition analysis by energy-dispersive spectroscopy (EDS) on as-grown crystals were performed using a Hitachi S8030 scanning electron microscope (SEM) equipped with a PGT energy-dispersive X-ray analyzer with an accelerating voltage of 15 kV and a 100 s accumulation time for data acquisition. The EDS analysis gave the atomic (K, Mo, and Ti) ratios for all three compounds, which were consistent with the formulas deduced by single-crystal XRD analysis (Figures S11−S13).

Thermal Analysis. Thermogravimetric analysis (TGA) and differential thermal analysis (DTA) were carried out with a NETZSCH-Proteus-61 analyzer instrument. Crystalline samples were placed in an alumina crucible and heated from room temperature to 800 °C at a rate of 10 °C/min and then cooled to room temperature at the same rate under flowing helium with a flow rate of 25 mL/min. The experimental results of weight loss before 200 °C are in agreement with the theoretical weight losses caused by the dehydration of these three compounds (Figure S14).

Magnetic Susceptibility. Magnetic measurements were performed on polycrystalline samples sealed in a polyethylene bag under a dinitrogen atmosphere. All data were collected using a Quantum Design MPMS-XL SQUID magnetometer from 1.8 to 300 K at an applied DC field of 1000 Oe. The negative, temperature-independent magnetic susceptibility measured for these three compounds indicates that they are diamagnetic. The very weak paramagnetic signals were attributed to the sample holder and minor impurities (Figure S15).

Raman Spectroscopy. The Raman spectra were collected on a Horiba LabRAM HR Evolution Confocal Raman System equipped with a solid-state laser of 473 nm.

Infrared (IR) Spectroscopy. The Fourier transform infrared (FTIR) spectra in the range from 400 to 4000 cm^{-1} were recorded on a Bruker 37 Tensor FTIR spectrometer at room temperature (Figure S16).

■ RESULTS AND DISCUSSION

Structure Determination. Owing to the similarity of their ionic radii and X-ray scattering factors, it is only possible to distinguish oxygen and fluorine atoms by X-ray diffraction in certain favorable, ordered cases. The three compounds in this work feature a common fundamental building block, an $[Mo_3X_{13}]$ cluster (X = O,F), which is depicted in Figure 3a.

In these cases, bond valence calculations fail to conclusively determine the oxygen and fluorine crystallographic sites on the cluster because of the presence of metal−metal bonds in the cluster. Given the experimentally diamagnetic properties of all

https://dx.doi.org/10.1021/jacs.0c04019
J. Am. Chem. Soc. 2020, 142, 12288−12298

three compounds, the triangular Mo_3 unit in the $[Mo_3X_{13}]$ cluster should exhibit a spin singlet state. With the additional observation of the dark-red color of the crystals and the intracluster Mo−Mo bond length, an oxidation state of 4+ for Mo was proposed. In this way, the six cluster d electrons can be paired in three Mo−Mo bonds in the cluster. Then, to achieve charge balance, there should be four oxygen atom sites and nine fluorine atom sites in the cluster (i.e., $[Mo_3O_4F_9]^{5-}$). On the basis of the aforementioned analysis, the asymmetric unit models of these three compounds were proposed (Figure 3b−d).

^{19}F NMR Crystallography. ^{19}F NMR spectroscopy directly probes the number of fluorine sites and their local crystallographic environment. ^{19}F NMR echo spectra of **1** and **2** show two groups of sharp resonances in Figure 4. The sharp line

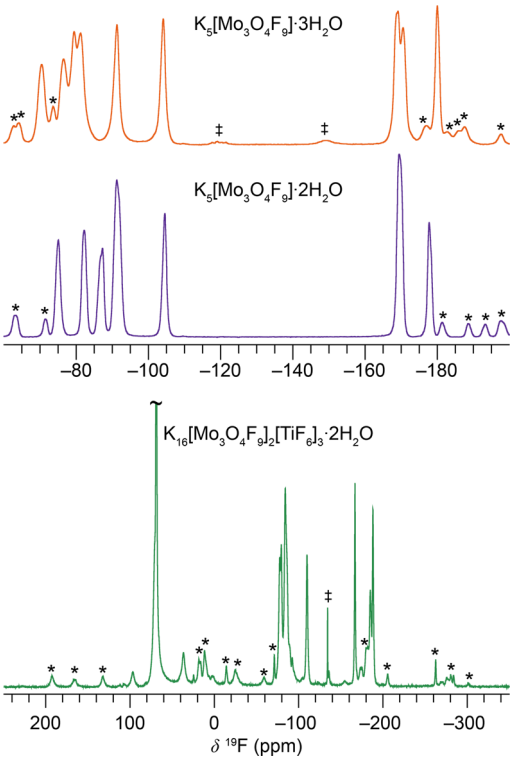

Figure 4. ^{19}F MAS NMR echo spectra of the three Mo cluster compounds. The MAS rates were 40 kHz for **1** and **2** and 33 kHz for **3**, depicted from top to bottom. Spinning side bands and impurity peaks are denoted with asterisks and crosses, respectively.

shapes immediately suggested the absence of oxygen/fluorine disorder that is characteristic of many oxyfluorides.[45−48] There are six isotropic resonances between −70 and −105 ppm and three isotropic resonances between −165 and −185 ppm. Additionally, a number of spinning side bands are present. There is some overlap between the isotropic resonances and the spinning side bands.

Variable MAS rates were used to identify the isotropic signals (Figure S1). Furthermore, the ^{19}F signals were sensitive to the small variations in temperature as a function of MAS rate; thus, recording spectra at several rates led to additional resolution and revealed the temperature dependence. Deconvolution of the spectra and fits of the side bands based on chemical shift anisotropy (CSA) are given in Figures S2−S4, and the resulting chemical shift tensor parameters (isotropic shift (δ_{iso}), CSA) are given in Tables 2−4. The chemical shift

Table 2. Experimental and Calculated ^{19}F NMR Shift Tensor of $K_5[Mo_3O_4F_9]\cdot 3H_2O$ (1)

	experimental		DFT	
F-atom assignment	δ_{iso} at 40 kHz MAS [±0.2] (ppm)	±CSA [±20] (ppm)	δ_{iso} (ppm)	CSA (ppm)
1	−91.3	130	−106	−103
2	−70.5	130	−66	−149
3	−79.5	150	−72	−168
4	−81.4	155	−85	−138
5	−104.2	110	−112	−117
6	−76.6	150	−70	−173
7[a]	−170.7	130	−173	99
8	−180.1	140	−177	94
9[a]	−168.9	130	−166	101

[a]Assigned by the temperature dependence.

Table 3. Experimental and Calculated ^{19}F NMR Shift Tensor of $K_5[Mo_3O_4F_9]\cdot 2H_2O$ (2)

	experimental		DFT	
F-atom assignment	δ_{iso} at 40 kHz MAS [±0.2] (ppm)	±CSA [±20] (ppm)	δ_{iso} (ppm)	CSA (ppm)
1	−91.2	120	−87	−144
2	−82.4	150	−83	−138
3	−92.1	140	−91	−130
4	−87.1	180	−84	−176
5	−104.6	140	−123	−118
6	−75.2	145	−76	−141
7[a]	−170.0	120	−170	108
8	−177.9	120	−176	90
9[a]	−169.3	120	−166	88

[a]Assigned by the temperature dependence.

Table 4. Experimental and Calculated ^{19}F NMR Shift Tensor of $K_{16}[Mo_3O_4F_9]_2[TiF_6]_3\cdot 2H_2O$ (3)

	experimental		DFT	
F-atom assignment	δ_{iso} at 33 kHz MAS [±0.2] (ppm)	±CSA [±20] (ppm)	δ_{iso} (ppm)	CSA (ppm)
1	−85.0	150	−80	−150
2	−87.0	150	−87	−138
3	−79.7	180	−82	−149
4	−77.2	100	−79	−146
5	−84.1	150	−78	−155
6	−110.5	120	−124	−117
7	−184.3	120	−184	74
8	−187.8	110	−183	112
9	−166.5	100	−161	111

asymmetry (η_{CSA}) parameter had a small but non-negligible effect on the fits, so precise values could not be determined. Typically, η_{CSA} = 0.5−1 gave the best fit; when η_{CSA} = 1, the sign of the CSA cannot be determined. Therefore, only the CSA magnitude was determined experimentally, as indicated by the ± CSA designation in the tables. The clear grouping into six high-frequency resonances and three low-frequency resonances suggested that these groups correspond to fluorines F1−F6 in the plane of the apical X-site oxygen (O_X) and fluorines F7−F9 in the plane of the bridging Y-site oxygen (O_Y) atoms, respectively. In **3**, the same two sets of resonances

https://dx.doi.org/10.1021/jacs.0c04019
J. Am. Chem. Soc. 2020, 142, 12288−12298

are present between −60 and −200 ppm and are again assigned to the three distinct F_Z−O_Y (F7−F9) and six distinct F_Z−O_X (F1−F6) fluorine atoms. The sharp nature of the resonances assigned to F1−F9 suggests that there is neither disorder nor exchange between any of these sites.

For **3**, additionally, there is a large resonance observed at 69 ppm and three smaller and relatively broad signals at 97, 71, and 37 ppm (Figure 4, Figure S5). On the basis of their position (*vide infra*) and intensity, these four resonances can be ascribed to the two TiF_6 octahedra interleaving the $[Mo_3O_4F_9]$ cluster in the extended structure. The signal at 69 ppm is assigned to F of the octahedra on the 4e Wyckoff site (F10−F15), and the signals at 97, 71, and 37 ppm are assigned to the octahedra on the 2b Wyckoff site, (F16−F18) on the basis of symmetry. The fluorine atoms of TiF_6 at the 4e site are crystallographically distinct, so six signals would be expected; the single resonance at 69 ppm suggests motional averaging of the six F positions. Furthermore, the full width at half-maximum (fwhm) of the signal at 69 ppm is 350 Hz (0.93 ppm), while the fwhm values of the peaks at 97, 71, and 37 ppm are 1800 Hz (4.8 ppm), 1690 Hz (4.5 ppm), and 1730 Hz (4.6 ppm), respectively, at ambient temperature (36 °C from MAS frictional heating). Variable-temperature spectra (Figure S6) of the TiF_6 resonances were recorded. As the temperature decreases, the resonance at 69 ppm broadens, reaching 1320 Hz (3.51 ppm) when the sample reaches −17 °C, which is nearly equivalent to the three unaveraged 2b resonances. Thus, line width analysis is a further indication of TiF_6 dynamics at the 4e site. These latter 2b TiF_6 fluorine atoms are apparently static from the NMR perspective (i.e., not exchanging) below ca. 20 °C; above this temperature, the shoulder above 70 ppm becomes more pronounced before all of the 2b signals broaden and nearly disappear toward higher temperatures. These data suggest that the 2b fluorine atoms are in an intermediate exchange regime at 75 °C. We note that the ^{19}F signal assigned to the 4e octahedra is located at 69 ppm and that the weighted average of the signals assigned to the 2b octahedra is 68 ppm; both are nearly identical to the potassium-coordinated $[TiF_6]^{2-}$ octahedra in K_2TiF_6, which exhibit a ^{19}F resonance at 71.5 ppm (Figure S7) with a fwhm of 3200 Hz (8.5 ppm). Finally, the spin−lattice relaxation time (T_1) for all signals in **1** and **2** is 5−10 s, while the T_1 of **3** is ∼0.6 s at 36 °C. The accelerated relaxation in **3** is another attribute of the TiF_6 dynamics leading to rapid fluctuations in the dipolar couplings. We recently observed this phenomenon of dynamically averaged MF_6 (M = Ti, Zr, Hf) octahedra in all three members of Δ,Λ-$[Cu(bpy)_2(H_2O)]_2[MF_6]_2 \cdot 3H_2O$.[49] The structural origins that confer dynamic averaging to some MF_6 octahedra but not others may be related to hydrogen bonding or electrostatic interactions and are the motivation for future study. Though it cannot fully account for the ^{19}F signal averaging due to symmetry considerations, some extent of the aforementioned line narrowing and enhanced relaxation on the ^{19}F MF_6 sites could result from dynamics of the structural water molecules and decreased ^1H−^{19}F dipolar coupling.

Ab initio NMR calculations were performed on the three crystal structures with the objective of verifying the assigned structural units and determining the assignment of individual fluorine sites within the groups. Solid-state NMR calculations can be used to distinguish potential structural models and challenging site assignments. Isotropic shieldings (σ_{iso}) are calculated and are converted to isotropic chemical shifts (δ_{iso}) according to the equation δ_{iso} [ppm] = −(0.824 ± 0.026)σ_{iso} [ppm] + (66 ± 6) [ppm], where errors are standard deviations (Figure S8). Computed chemical shift tensor parameters are given in Tables 2−4. Calculated shifts for sites such as **1** (F1 and F5), **2** (F5), and **3** (F6) are significantly more negative than experimentally observed; these sites are all associated with relatively short F---H distances between cluster F atoms and water H atoms, which may indicate the dynamics of the structural water under experimental conditions that are not captured by the static DFT calculations.

The DFT calculations unambiguously confirm the assignment of the F_Z−O_X sites to F1−F6 and the F_Z−O_Y sites to F7−F9 in all three compounds. Furthermore, the computed shifts enable the assignment of individual signals within F_Z−O_Y and F_Z−O_X; the temperature dependence of each signal and the 0 K temperature of DFT must be considered. Finally, ^{19}F−^{19}F dipolar-coupling-mediated measurements were used to probe spatial relationships, which was particularly useful for determining sites within the $Mo_3O_4F_9$ cluster of $K_{16}[Mo_3O_4F_9]_2[TiF_6]_3 \cdot 2H_2O$ (Figure 5, Figure S9).

A correlation between the Mo−F distance and δ_{iso} ^{19}F was observed across the series of compounds (Figure 6). The chemical shifts increase as the bond distances decrease with a sensitivity on the order of 0.01 Å, with structural differences

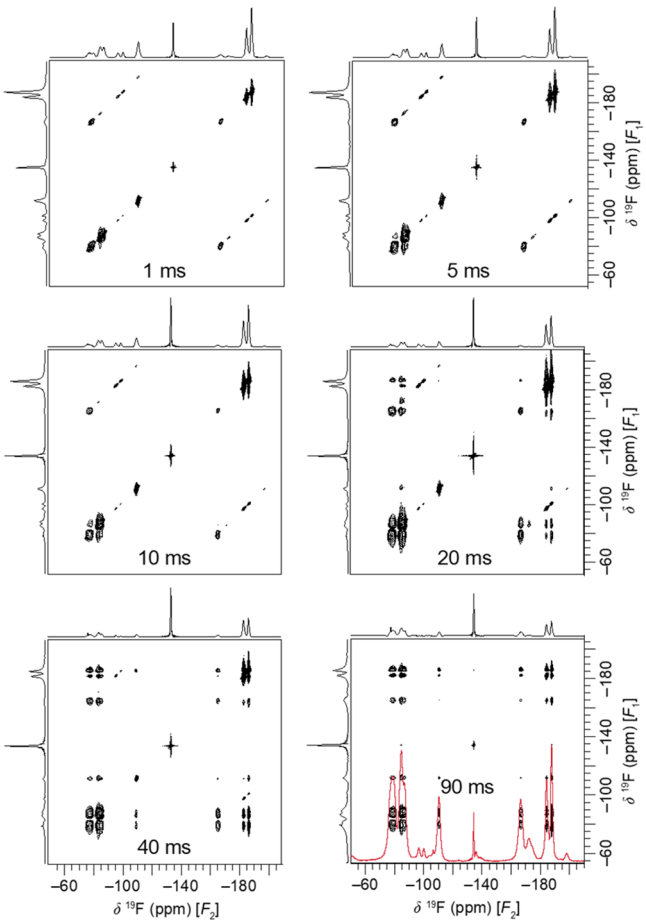

Figure 5. ^{19}F−^{19}F spin exchange spectra of $K_{16}[Mo_3O_4F_9]_2[TiF_6]_3 \cdot 2H_2O$ (**3**). Correlation peaks were measured as a function of mixing time, as indicated in each panel, at 33 kHz MAS. A 1D spectrum is overlaid on the 2D spectrum in the bottom right panel. For a more detailed spectral assignment, see Supporting Information Figure S9 and the associated text.

https://dx.doi.org/10.1021/jacs.0c04019
J. Am. Chem. Soc. 2020, 142, 12288−12298

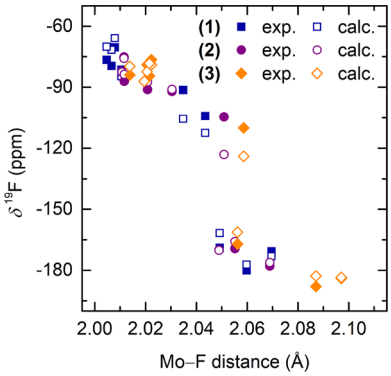

Figure 6. Experimental and calculated ^{19}F chemical shifts as a function of the Mo−F bond distance. DFT calculations of ^{19}F shifts were performed after relaxation of the lattice parameters and atomic positions. For the effects of relaxed vs constrained lattice parameters for **3**, see Supporting Information Figure S10.

leading to second-order offsets in the trend. This was observed in both experimental and calculated shifts as the bonds lengthened as a function of lattice expansion (Figure 6, Figure S10). We attribute this behavior to the magnetic-field-induced paramagnetic contribution to chemical shielding as originally described by Ramsey, Saika, and Slichter.[50−52] This early work established the orbital motion of the valence electrons as the primary source of the chemical shift range in ^{19}F and laid the theory for its bond length dependence in the form of the distance between the nucleus and the valence p electrons. As discussed recently for ^{19}F shifts in TiF_4, the paramagnetic contribution decreases as the M−F bond distance increases.[53] This work indicates that this is a more general trend that applies even for fluorine in a complex oxyfluoride cluster where it is bound to d^2 Mo^{4+} participating in metal−metal bonding.

The generality and sensitivity of ^{19}F paramagnetic shielding to small changes in bond distance, on the order of 0.01 Å or less, make it a powerful probe of crystal structure, particularly when experimental spectra are analyzed with insights from computational modeling. In this work, the sensitivity of the chemical shift to the Mo−F bond length can also explain the small differences in the ^{19}F MAS NMR echo spectra within the clusters for **1** vs **2** vs **3** (Figure 4, Figure S1), given the small differences in intracluster Mo−F bond lengths (Table 5). The NMR and X-ray data were supplemented by experimental (Figure S16) and computed (Figure S17) IR and Raman spectroscopy, confirming the oxocluster nature of all three compounds.

Structure Description. These three phases contain similar discrete $[Mo_3O_4F_9]$ clusters (Figure 7). In the $[Mo_3O_4F_9]$ cluster, three Mo atoms form an almost equilateral triangle with one central apical μ_3-O ligand residing on the C_3 axis above the Mo_3 plane. The bond lengths of Mo-(μ_3-O) are between 2.030(2) and 2.047(3) Å. Each pair of Mo atoms is bridged by a μ_2-O ligand with the Mo-(μ_2-O) distance ranging from 1.919(5) to 1.940(7) Å, forming an O_3 plane which is parallel to the Mo_3 plane. In addition, each Mo atom also bonds to three terminal F ligands with the Mo−F bond lengths ranging from 2.006 to 2.082 Å, which radiate away from the core of the cluster. Interestingly, those three terminal F ligands above the Mo_3 plane feature a coplanar arrangement while the other six terminal F ligands on the other side also form a parallel plane. These Mo−O and Mo−F distances are consistent with those observed in other fluorine−molybdenum-cluster-containing compounds.[23,28] The intracluster Mo−Mo distances are listed in Table 5. As we know, bond lengths that are shorter than the sum of the covalent radii are a reliable indication of metal−metal bonding. The short Mo−Mo separations suggest Mo−Mo bonds in the structure, and this is supported by our spectroscopic measurements (Figures S16 and S17). Similar Mo−Mo bond lengths were also observed in other molybdenum cluster compounds.[28,29]

Table 5. Intracluster Mo−Mo and Mo−F Bond Lengths of 1, 2, and 3

$K_5[Mo_3O_4F_9]\cdot 3H_2O$ (**1**)		$K_5[Mo_3O_4F_9]\cdot 2H_2O$ (**2**)		$K_{16}[Mo_3O_4F_9]_2[TiF_6]_3\cdot 2H_2O$ (**3**)	
atom pair	bond length (Å)	atom pair	bond length (Å)	atom pair	bond length (Å)
Mo1−Mo2	2.516	Mo1−Mo2	2.497	Mo1−Mo2	2.504
Mo1−Mo3	2.499	Mo1−Mo3	2.491	Mo1−Mo3	2.497
Mo2−Mo3	2.517	Mo2−Mo3	2.512	Mo2−Mo3	2.500
F1−Mo3	2.040	F1−Mo1	2.021	F1−Mo1	2.009
F2−Mo1	2.011	F2−Mo1	2.011	F2−Mo1	2.014
F3−Mo1	2.014	F3−Mo3	2.031	F3−Mo2	2.014
F4−Mo2	2.017	F4−Mo3	2.012	F4−Mo2	2.006
F5−Mo2	2.050	F5−Mo2	2.051	F5−Mo3	2.006
F6−Mo3	2.009	F6−Mo2	2.011	F6−Mo3	2.055
F7−Mo3	2.074	F7−Mo1	2.049	F7−Mo1	2.082
F8−Mo1	2.066	F8−Mo3	2.069	F8−Mo2	2.080
F9−Mo1	2.056	F9−Mo2	2.055	F9−Mo3	2.048

Compound **1** crystallizes in monoclinic space group $P2_1/c$, with a unit cell of a = 13.121(3) Å, b = 7.928(2) Å, c = 14.928(4) Å, and β = 97.4(10)°. Four cluster anions, 20 potassium cations, and 12 free water molecules are contained in a unit cell. Compound **2** crystallizes in monoclinic space group $P2_1/n$, with a unit cell of a = 7.424(4) Å, b = 12.084(5) Å, c = 16.085(8) Å, and β = 91.6(2)°. The symmetry of **2** is different because of one less formula unit of water in the structure compared to the number in **1**. We find that **3** accommodates anionic octahedral $[TiF_6]^{2-}$. The compound crystallizes into monoclinic space group $P2_1/n$, with a unit cell of a = 6.313(4) Å, b = 24.686(15) Å, c = 14.621(9) Å, and β = 94.5(2)°. There are two formula units per cell. It is interesting that the two octahedral $[TiF_6]^{2-}$ on crystallographically distinct sites exhibit different symmetry. One type of octahedron sits on the 4e Wyckoff site and is distorted, while the other type is on the 2b Wyckoff site and is nondistorted. The potassium ions provide compensating positive charges in the structure and are located between adjacent clusters. Meanwhile, the free molecular water is located between the cluster units, forming hydrogen bonds between the dangling fluorine atoms and the hydrogen atoms of the H_2O in the structure. The hydrogen bond lengths are in the range of 1.820 to 1.940 Å.

Molecular Orbital Description of the $[Mo_3O_4F_9]^{5-}$ Cluster. A qualitative understanding of the bonding scheme in the trimeric $[Mo_3O_4F_9]^{5-}$ cluster can be initiated by considering an idealized collateral trioctahedral model. For each octahedron, the e_g ($4d_{z^2}$, $4d_{x^2-y^2}$), a_{1g} (5s), and t_{1u} ($5p_x$, $5p_y$, $5p_z$) orbitals combine with the ligand group orbitals of matching symmetry to form six occupied σ-bonding orbitals. Once the octahedral σ-bonding frameworks are established for each metal−ligand octahedron, we next consider the three t_{2g} nonbonding orbitals of each metal. As a result of the metal−metal bonds among the three molybdenum cations in the

https://dx.doi.org/10.1021/jacs.0c04019
J. Am. Chem. Soc. 2020, 142, 12288−12298

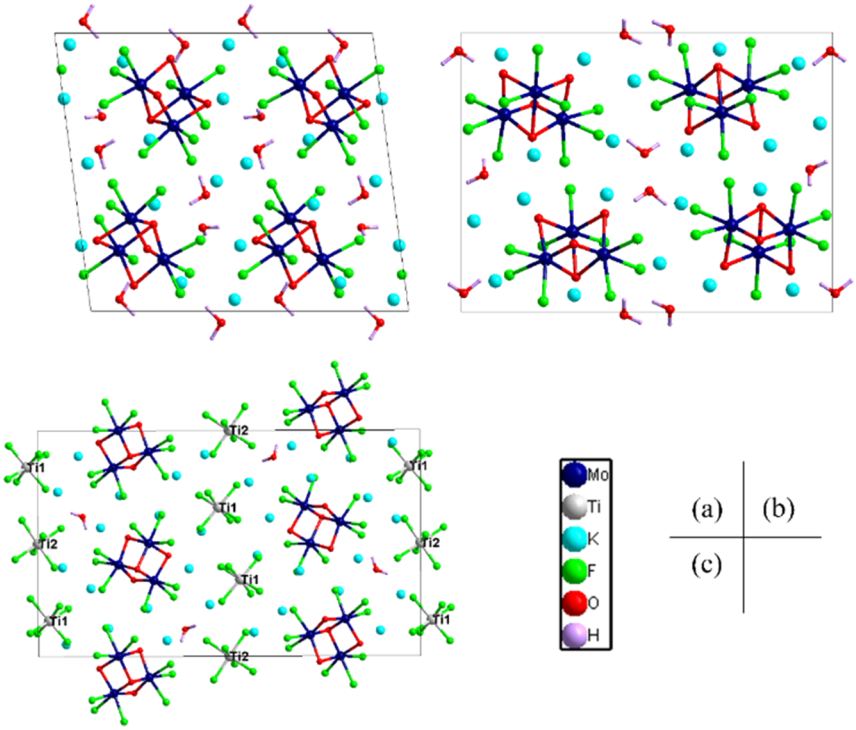

Figure 7. Ball-and-stick representation of compounds (a) **1**, (b) **2**, and (c) **3**.

$[Mo_3O_4F_9]^{5-}$ cluster, which has C_{3v} symmetry, the nine t_{2g} orbitals (three sets of $4d_{xy}$, $4d_{yz}$, and $4d_{xz}$) form molecular orbitals (MO). The reducible representation for these nine t_{2g} orbitals is given in Table S1 (with the C_{3v} character table) and can be reduced to $2A_1 + A_2 + 3E$. The three d_{xz} orbitals combine and give one bonding MO of A_1 symmetry and a doubly degenerate antibonding MO with E symmetry. Similarly, three d_{xy} orbitals form another A_1 bonding molecular orbital and another pair of E antibonding orbitals, while three d_{yz} orbitals form an A_2 antibonding and a doubly degenerate E pair of bonding orbitals. Six d electrons in each Mo_3 core comprise three electron pairs, which fill three bonding molecular orbitals, 1a and doubly degenerate 1e (Figure 8a), giving the cluster a metal−metal bond order of 1. The electronic ground state of the $[Mo_3]^{12+}$ cluster is then $1a^21e^4$ and forms an $S = 0$ spin state with the electrons delocalized over the triangular unit. This electron distribution can be discerned from the real-space representation of the occupied $1a_1$ and 1e molecular orbitals shown in Figure 8b. Compounds **1**, **2**, and **3** are the first 4d transition-metal compounds, to the best of our knowledge, to display triangular orbital molecules[54] within a crystal phase arising from a trimeric spin singlet state between Mo^{4+} ions in the $[Mo_3]^{12+}$ cluster. 3d Transition-metal compound analogues exist, and the same six-electron spin singlet species arises from V−V single bonds in the triangular $(V^{3+})_3$ (t_{2g}^2 configuration) orbital molecules in A_xVO_2 and $BaV_{10}O_{15}$.[54] This $S = 0$ state is in agreement with the results of the negative and temperature-independent magnetic susceptibilities, which show diamagnetic responses in all three compounds.

To analyze the bonding within the cluster in more detail, electronic structure calculations were performed. The density of states of **3** resolved by species and angular momentum is shown in Figure 8c. The states located between −6.7 and −3 eV are dominated by the 2p orbitals of the ligands (O and F), with small contributions from Ti and Mo d orbitals. Hybridization of these states through metal−ligand bonding stabilize the compound. The two Mo-dominated peaks between −2 and 0 eV correspond directly to the $1a_1$ and 1e orbitals deduced from our symmetry-derived MO diagram (Figure 8a), which are also visualized in Figure 8b. This assignment is based on the ratio of the peak heights and an analysis of the Kohn−Sham wave functions corresponding to those peaks. The wave functions clearly show that these orbitals arise from metal−metal bonding interactions.

■ CONCLUSIONS

Three oxyfluorides containing the trinuclear cluster $[Mo_3O_4F_9]^{5-}$ were obtained by hydrosolvothermal synthesis. The structures of these compounds were elucidated by combining single-crystal X-ray diffraction and solid-state ^{19}F NMR spectroscopy supported by *ab initio* calculations. The crystallographic sites of the fluorine atoms in these structures were assigned, and no site disorder was observed. The generality and sensitivity of ^{19}F paramagnetic shielding to small changes in bond distance, on the order of 0.01 Å or less, make this multimodal analysis approach a powerful structural probe. Characterization via Raman and infrared spectroscopies confirm the structural details, particularly for the proposed heteroanion arrangement and structural water in this series of compounds. The NMR spectroscopy also revealed unexpected fluorine dynamics within the $[TiF_6]^{2-}$ units. Qualitative discussion of the molecular orbitals is used to explain the bonding in these compounds. The average Mo−Mo distance of 2.505 Å and the diamagnetism of these three compounds can be attributed to a metal−metal bond order of unity. The electronic ground state of the cluster is $1a^21e^4$, and all compounds exhibit a trimeric spin-singlet state. We believe that the combination of X-ray diffraction and ^{19}F NMR

https://dx.doi.org/10.1021/jacs.0c04019
J. Am. Chem. Soc. 2020, 142, 12288−12298

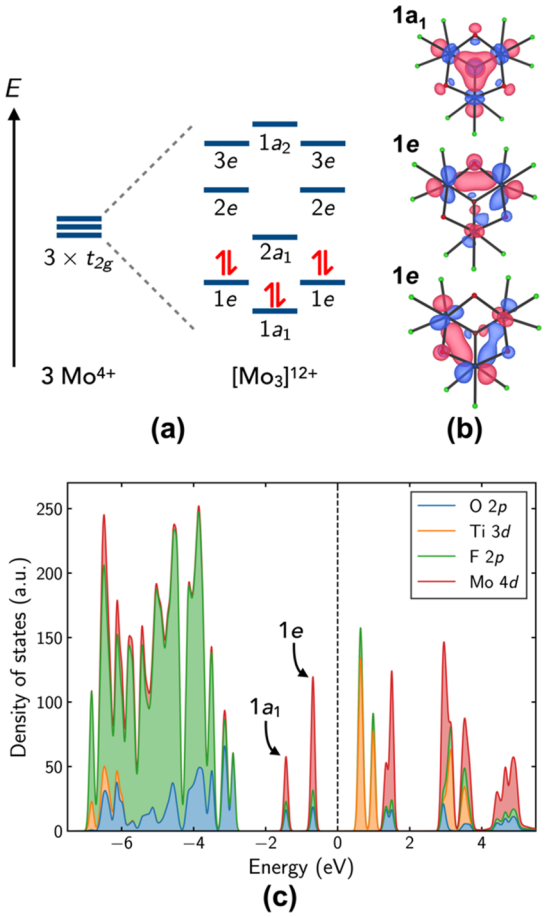

Figure 8. (a) Schematic view of the molecular orbitals formed in a $[Mo_3]^{12+}$ trimer with the ground-state electron configuration; (b) real-space $1a_1$ and 1e molecular orbitals; and (c) stacked projected density of states (PDOS) for structure **3**. The Fermi level (dashed line) separates occupied from unoccupied states. The element and orbital contributions to the DOS are proportional to the shaded area in the plot. Contributions from potassium and hydrogen are negligible in this range and are omitted. The large number of states between −6.7 and −3 eV is dominated by O 2p and F 2p states hybridized with Mo 4d orbitals, forming metal−ligand bonding states. The two Mo-dominated peaks between −2 and 0 eV are the $1a_1$ and 1e bonding orbitals (shown in (b)) responsible for metal−metal bonding.

crystallography provides a powerful tool for the study of both inorganic and organic fluoride and oxyfluoride materials.

■ ASSOCIATED CONTENT

Supporting Information

The Supporting Information is available free of charge at https://pubs.acs.org/doi/10.1021/jacs.0c04019.

Additional NMR spectra, including ^{19}F chemical shifts as a function of MAS rate and temperature as well as deconvolution and CSA fitting; EDS spectra and TG−DTA curves; experimental infrared and Raman spectra; calculated phonon density of states (PDF)

CIFs of **1** $K_5[Mo_3O_4F_9]\cdot 3H_2O$, **2** $K_5[Mo_3O_4F_9]\cdot 2H_2O$, and **3** $K_{16}[Mo_3O_4F_9]_2[TiF_6]_3\cdot 2H_2O$ (both 100 K and 296 K for **3**) (CIF)

■ AUTHOR INFORMATION

Corresponding Authors

Andrew J. Morris − *School of Metallurgy and Materials, University of Birmingham, Edgbaston, Birmingham B15 2TT, U.K.;* orcid.org/0000-0001-7453-5698; Email: A.J.Morris.1@bham.ac.uk

James M. Rondinelli − *Department of Materials Science and Engineering, Northwestern University, Evanston, Illinois 60208, United States;* orcid.org/0000-0003-0508-2175; Email: jrondinelli@northwestern.edu

Kenneth R. Poeppelmeier − *Department of Chemistry, Northwestern University, Evanston, Illinois 60208, United States;* orcid.org/0000-0003-1655-9127; Email: krp@northwestern.edu

Authors

Fenghua Ding − *Department of Chemistry, Northwestern University, Evanston, Illinois 60208, United States;* orcid.org/0000-0002-9529-3023

Kent J. Griffith − *Department of Chemistry, Northwestern University, Evanston, Illinois 60208, United States;* orcid.org/0000-0002-8096-906X

Can P. Koçer − *Theory of Condensed Matter Group, Cavendish Laboratory, University of Cambridge, Cambridge CB3 0HE, U.K.;* orcid.org/0000-0003-0477-5148

Richard J. Saballos − *Department of Materials Science and Engineering, Northwestern University, Evanston, Illinois 60208, United States*

Yiran Wang − *Department of Chemistry, Northwestern University, Evanston, Illinois 60208, United States*

Chi Zhang − *Department of Materials Science and Engineering, Northwestern University, Evanston, Illinois 60208, United States*

Matthew L. Nisbet − *Department of Chemistry, Northwestern University, Evanston, Illinois 60208, United States;* orcid.org/0000-0001-9531-9193

Complete contact information is available at: https://pubs.acs.org/10.1021/jacs.0c04019

Author Contributions

$^{\perp}$F.D. and K.J.G. contributed equally. The manuscript was written through the contributions of all authors. All authors have given approval to the final version of the manuscript.

Notes

The authors declare no competing financial interest.

CCDC 1979703−1979705 and 1987370 contain the supplementary crystallographic data for this paper. These data can be obtained free of charge via www.ccdc.cam.ac.uk/data_request/cif, or by emailing data_request@ccdc.cam.ac.uk, or by contacting The Cambridge Crystallographic Data Centre, 12 Union Road, Cambridge CB2 1EZ, UK; fax: + 44 1223 336033.

■ ACKNOWLEDGMENTS

This work was supported by funding from the National Science Foundation (DMR-1904701). K.J.G. was supported by the Joint Center for Energy Storage Research (JCESR), an Energy Innovation Hub funded by the U.S. Department of Energy, Office of Science, Office of Basic Energy Sciences. R.J.S., J.M.R., and powder diffraction at the J. B. Cohen X-ray Diffraction Facility were supported by the MRSEC program (DMR-1720139) at the Materials Research Center of North-

western University (NU). Single-crystal X-ray, solid-state NMR, and FT-IR measurements were acquired at Northwestern University's Integrated Molecular Structure Education and Research Center (IMSERC), which is supported by grants from NSF-NSEC, NSF-MRSEC, NSF DMR-0521267, the KECK Foundation, the State of Illinois, and NU. Raman and EDS measurements made use of the EPIC and SPID facilities of NU's NU*ANCE* Center, which has received support from the Soft and Hybrid Nanotechnology Experimental (SHyNE) Resource (NSF ECCS-1542205), the MRSEC program, the International Institute for Nanotechnology (IIN), the Keck Foundation, and the State of Illinois through the IIN. Computations were performed using the Extreme Science and Engineering Discovery Environment (XSEDE) Stampede 2 at the Texas Advance Computing Center (allocation TG-DMR110085), which is supported by NSF grant number ACI-1548562 and also Athena at HPC Midlands+, which was funded by the EPSRC through grant EP/P020232/1 (via the EPSRC RAP call of spring 2019). C.P.K. thanks the Winton Programme for the Physics of Sustainability and EPSRC for financial support.

■ REFERENCES

(1) Kageyama, H.; Hayashi, K.; Maeda, K.; Attfield, J. P.; Hiroi, Z.; Rondinelli, J. M.; Poeppelmeier, K. R. Expanding frontiers in materials chemistry and physics with multiple anions. *Nat. Commun.* **2018**, *9*, 772.

(2) Harada, J. K.; Charles, N.; Poeppelmeier, K. R.; Rondinelli, J. M. Heteroanionic Materials by Design: Progress Toward Targeted Properties. *Adv. Mater.* **2019**, *31*, 1805295.

(3) Pan, C.; Yang, X.; Xiong, L.; Lu, Z.; Zhen, B.; Sui, X.; Deng, X.; Chen, L.; Wu, L. Solid-State Nonlinear Optical Switch with the Widest Switching Temperature Range Owing to its Continuously Tunable Tc. *J. Am. Chem. Soc.* **2020**, *142*, 6423−6431.

(4) Ding, Q.; Liu, X.; Zhao, S.; Wang, Y.; Li, Y.; Li, L.; Liu, S.; Lin, Z.; Hong, M.; Luo, J. Designing a Deep-UV Nonlinear Optical Fluorooxosilicophosphate. *J. Am. Chem. Soc.* **2020**, *142*, 6472−6476.

(5) Yu, H.; Nisbet, M. L.; Poeppelmeier, K. R. Assisting the effective design of polar iodates with early transition-metal oxide fluoride anions. *J. Am. Chem. Soc.* **2018**, *140*, 8868−8876.

(6) Shi, G.; Wang, Y.; Zhang, F.; Zhang, B.; Yang, Z.; Hou, X.; Pan, S.; Poeppelmeier, K. R. Finding the Next Deep-Ultraviolet Nonlinear Optical Material: $NH_4B_4O_6F$. *J. Am. Chem. Soc.* **2017**, *139*, 10645−10648.

(7) Lee, J.; Kitchaev, D. A.; Kwon, D.; Lee, C.; Papp, J. K.; Liu, Y.; Lun, Z.; Clément, R. J.; Shi, T.; McCloskey, B. D. Reversible Mn^{2+}/Mn^{4+} double redox in lithium-excess cathode materials. *Nature* **2018**, *556*, 185−190.

(8) Clément, R.; Lun, Z.; Ceder, G. Cation-disordered rocksalt transition metal oxides and oxyfluorides for high energy lithium-ion cathodes. *Energy Environ. Sci.* **2020**, *13*, 345−373.

(9) Kim, M.; Kim, D.; Lee, W.; Jang, H. M.; Kang, B. New class of 3.7 V Fe-based positive electrode materials for Na-Ion battery based on cation-disordered polyanion framework. *Chem. Mater.* **2018**, *30*, 6346−6352.

(10) Kibsgaard, J.; Jaramillo, T. F.; Besenbacher, F. Building an appropriate active-site motif into a hydrogen-evolution catalyst with thiomolybdate $[Mo_3S_{13}]^{2-}$ clusters. *Nat. Chem.* **2014**, *6*, 248−253.

(11) Ji, Z.; Trickett, C.; Pei, X.; Yaghi, O. M. Linking Molybdenum−Sulfur Clusters for Electrocatalytic Hydrogen Evolution. *J. Am. Chem. Soc.* **2018**, *140*, 13618−13622.

(12) Llusar, R.; Uriel, S.; Vicent, C.; Clemente-Juan, J. M.; Coronado, E.; Gómez-García, C. J.; Braïda, B.; Canadell, E. Single-component magnetic conductors based on Mo_3S_7 trinuclear clusters with outer dithiolate ligands. *J. Am. Chem. Soc.* **2004**, *126*, 12076−12083.

(13) Perrin, C.; Cordier, S.; Gulo, F.; Perrin, A. The octahedral cluster compounds of early transition metals: An original class of dielectric materials. *Ferroelectrics* **2001**, *254*, 83−90.

(14) Lancry, E.; Levi, E.; Gofer, Y.; Levi, M.; Salitra, G.; Aurbach, D. Leaching chemistry and the performance of the Mo_6S_8 cathodes in rechargeable Mg batteries. *Chem. Mater.* **2004**, *16*, 2832−2838.

(15) Chae, M. S.; Heo, J. W.; Lim, S.; Hong, S. Electrochemical zinc-ion intercalation properties and crystal structures of $ZnMo_6S_8$ and $Zn_2Mo_6S_8$ chevrel phases in aqueous electrolytes. *Inorg. Chem.* **2016**, *55*, 3294−3301.

(16) Geng, L.; Scheifers, J. P.; Zhang, J.; Bozhilov, K. N.; Fokwa, B. P.; Guo, J. Crystal Structure Transformation in Chevrel Phase Mo_6S_8 Induced by Aluminum Intercalation. *Chem. Mater.* **2018**, *30*, 8420−8425.

(17) Juran, T. R.; Smeu, M. Hybrid density functional theory modeling of Ca, Zn, and Al ion batteries using the Chevrel phase Mo_6S_8 cathode. *Phys. Chem. Chem. Phys.* **2017**, *19*, 20684−20690.

(18) Gushchin, A. L.; Ooi, B. L.; Harris, P.; Vicent, C.; Sokolov, M. N. Synthesis and Characterization of Mixed Chalcogen Triangular Complexes with New $Mo_3(\mu_3\text{-S})(\mu_2\text{-Se}_2)_3^{4+}$ and $M_3(\mu_3\text{-S})(\mu_2\text{-Se})_3^{4+}$ (M= Mo, W) Cluster Cores. *Inorg. Chem.* **2009**, *48*, 3832−3839.

(19) Fedin, V. P.; Sokolov, M. N.; Dybtsev, D. N.; Gerasko, O. A.; Virovets, A. V.; Fenske, D. Supramolecular assemblies of $[Mo_3Se_4Cl_x(H_2O)_{9-x}]^{(4-x)+}$ with cucurbituril; complementarity control through the variation of *x*. *Inorg. Chim. Acta* **2002**, *331*, 31−38.

(20) Shibahara, T. Cubane and incomplete cubane-type molybdenum and tungsten oxo/sulfido clusters. *Advances in Inorganic Chemistry*; Elsevier: 1991; Vol. *37*, pp 143−173.

(21) Cotton, F. A. Metal atom clusters in oxide systems. *Inorg. Chem.* **1964**, *3*, 1217−1220.

(22) Haraguchi, Y.; Michioka, C.; Imai, M.; Ueda, H.; Yoshimura, K. Spin-liquid behavior in the spin-frustrated Mo_3 cluster magnet $Li_2ScMo_3O_8$ in contrast to magnetic ordering in isomorphic $Li_2InMo_3O_8$. *Phys. Rev. B: Condens. Matter Mater. Phys.* **2015**, *92*, 014409.

(23) Sheckelton, J. P.; Neilson, J. R.; Soltan, D. G.; McQueen, T. M. Possible valence-bond condensation in the frustrated cluster magnet $LiZn_2Mo_3O_8$. *Nat. Mater.* **2012**, *11*, 493−496.

(24) Gheller, S. F.; Hambley, T. W.; Brownlee, R. T.; O'Connor, M. J.; Snow, M. R.; Wedd, A. G. Applications of molybdenum-95 NMR spectroscopy. 7. Studies of metal−metal bonded systems including aqueous molybdenum(IV) and molybdenum(V). Crystal and molecular structure of $Na_2[Mo_3O_4((O_2CCH_2)_2NCH_3)_3]\cdot 7H_2O$. *J. Am. Chem. Soc.* **1983**, *105*, 1527−1532.

(25) Samsonenko, D.; Virovets, A.; Sharonova, A.; Fedin, V.; Fenske, D. Synthesis and the crystal structure of a supramolecular adduct of the $[Mo_3O_4(H_2O)_6Cl_3]^+$ cluster complex with macrocyclic cavitand cucurbituril. *Russ. Chem. Bull.* **2001**, *50*, 494−496.

(26) Brorson, M.; Hazell, A.; Jacobsen, C. J.; Schmidt, I.; Villadsen, J. Preparation and Crystal Structures of Formato Complexes of the $[M^{IV}{}_3O_4]^{4+}$ and $[M^{IV}{}_3S_4]^{4+}$ (M= Mo, W) Clusters. Convenient Precursors to the Corresponding Aqua Complexes. *Inorg. Chem.* **2000**, *39*, 1346−1350.

(27) Kathirgamanathan, P.; Soares, A. B.; Richens, D. T.; Sykes, A. G. Effect of equivalent and nonequivalent sites on the kinetics of equilibration of thiocyanate with molybdenum oxide hydrate ($[Mo_3O_4(H_2O)_9]^{4+}$). *Inorg. Chem.* **1985**, *24*, 2950−2954.

(28) Müller, A.; Ruck, A.; Dartmann, M.; Reinsch-Vogell, U. MoIV in Aqueous Solutions: The Trinuclear Cluster $[Mo^{IV}O_4F_9]^{5-}$, the First Species Isolated from Mineral Acid Solution. *Angew. Chem., Int. Ed. Engl.* **1981**, *20*, 483−484.

(29) Müller, A.; Jostes, R.; Cotton, F. A. Trinuclear clusters of the early transition elements. *Angew. Chem., Int. Ed. Engl.* **1980**, *19*, 875−882.

(30) Mattes, R.; Mennemann, K.; Jäckel, N.; Rieskamp, H.; Brockmeyer, H.-J. Structure and properties of the fluorine-rich oxofluoromolybdates $Cs_3[Mo_2O_6F_3]$, $(NH_4)_3[Mo_2O_2F_9]$ and $(NH_4)_2[MoOF_5]$. *J. Less-Common Met.* **1980**, *76*, 199−212.

https://dx.doi.org/10.1021/jacs.0c04019
J. Am. Chem. Soc. 2020, 142, 12288−12298

(31) Kirsch, J. E.; Izumi, H. K.; Stern, C. L.; Poeppelmeier, K. R. Synthesis and characterization of the face-sharing bioctahedral $[Mo_2O_6F_3]^{3-}$ anion. *Inorg. Chem.* **2005**, *44*, 4586−4593.
(32) Bryce, D. L. NMR crystallography: structure and properties of materials from solid-state nuclear magnetic resonance observables. *IUCrJ* **2017**, *4*, 350−359.
(33) *SAINT*, v. A; Bruker Analytical X-ray Instruments, Inc.: Madison, WI, 2008.
(34) Dolomanov, O. V.; Bourhis, L. J.; Gildea, R. J.; Howard, J. A.; Puschmann, H. OLEX2: a complete structure solution, refinement and analysis program. *J. Appl. Crystallogr.* **2009**, *42*, 339−341.
(35) Spek, A. L. Single-crystal structure validation with the program PLATON. *J. Appl. Crystallogr.* **2003**, *36*, 7−13.
(36) Beckmann, P. A.; Dybowski, C. A Thermometer for Nonspinning Solid-State NMR Spectroscopy. *J. Magn. Reson.* **2000**, *146*, 379−380.
(37) Bielecki, A.; Burum, D. P. Temperature dependence of ^{207}Pb MAS spectra of solid lead nitrate. an accurate, sensitive thermometer for variable-temperature MAS. *J. Magn. Reson., Ser. A* **1995**, *116*, 215−220.
(38) Clark, S. J.; Segall, M. D.; Pickard, C. J.; Hasnip, P. J.; Probert, M. I.; Refson, K.; Payne, M. C. First principles methods using CASTEP. *Z. Kristallogr. - Cryst. Mater.* **2005**, *220*, 567−570.
(39) Perdew, J. P.; Burke, K.; Ernzerhof, M. Generalized gradient approximation made simple. *Phys. Rev. Lett.* **1996**, *77*, 3865.
(40) Vanderbilt, D. Soft self-consistent pseudopotentials in a generalized eigenvalue formalism. *Phys. Rev. B: Condens. Matter Mater. Phys.* **1990**, *41*, 7892.
(41) Monkhorst, H. J.; Pack, J. D. Special points for Brillouin-zone integrations. *Phys. Rev. B* **1976**, *13*, 5188.
(42) Yates, J. R.; Pickard, C. J.; Mauri, F. Calculation of NMR chemical shifts for extended systems using ultrasoft pseudopotentials. *Phys. Rev. B: Condens. Matter Mater. Phys.* **2007**, *76*, 024401.
(43) Pickard, C. J.; Mauri, F. All-electron magnetic response with pseudopotentials: NMR chemical shifts. *Phys. Rev. B: Condens. Matter Mater. Phys.* **2001**, *63*, 245101.
(44) Morris, A. J.; Nicholls, R. J.; Pickard, C. J.; Yates, J. R. OptaDOS: A tool for obtaining density of states, core-level and optical spectra from electronic structure codes. *Comput. Phys. Commun.* **2014**, *185*, 1477−1485.
(45) Dabachi, J.; Body, M.; Galven, C.; Boucher, F.; Legein, C. Preparation-Dependent Composition and O/F Ordering in NbO_2F and TaO_2F. *Inorg. Chem.* **2017**, *56*, 5219−5232.
(46) Griffin, J. M.; Yates, J. R.; Berry, A. J.; Wimperis, S.; Ashbrook, S. E. High-resolution ^{19}F MAS NMR spectroscopy: structural disorder and unusual J couplings in a fluorinated hydroxy-silicate. *J. Am. Chem. Soc.* **2010**, *132*, 15651−15660.
(47) Du, L. S.; Wang, F.; Grey, C. P. High−Resolution ^{19}F MAS and ^{19}F−^{113}Cd REDOR NMR Study of Oxygen/Fluorine Ordering in Oxyfluorides. *J. Solid State Chem.* **1998**, *140*, 285−294.
(48) Du, L. S.; Samoson, A.; Tuherm, T.; Grey, C. P. ^{19}F/^{23}Na double resonance MAS NMR study of oxygen/fluorine ordering in the oxyfluoride $Na_5W_3O_9F_5$. *Chem. Mater.* **2000**, *12*, 3611−3616.
(49) Nisbet, M. L.; Pendleton, I. M.; Nolis, G. M.; Griffith, K. J.; Schrier, J.; Cabana, J.; Norquist, A. J.; Poeppelmeier, K. R. Machine-learning-assisted Synthesis of Polar Racemates. *J. Am. Chem. Soc.* **2020**, *142*, 7555−7566.
(50) Ramsey, N. F. Magnetic shielding of nuclei in molecules. *Phys. Rev.* **1950**, *78*, 699.
(51) Ramsey, N. F. Chemical effects in nuclear magnetic resonance and in diamagnetic susceptibility. *Phys. Rev.* **1952**, *86*, 243.
(52) Saika, A.; Slichter, C. A note on the fluorine resonance shifts. *J. Chem. Phys.* **1954**, *22*, 26−28.
(53) Murakami, M.; Noda, Y.; Takegoshi, K. Terminal and bridging fluorine ligands in TiF_4 as studied by ^{19}F NMR in solids. *Solid State Nucl. Magn. Reson.* **2019**, *101*, 82−88.
(54) Attfield, J. P. Orbital molecules in electronic materials. *APL Mater.* **2015**, *3*, 041510.

https://dx.doi.org/10.1021/jacs.0c04019
J. Am. Chem. Soc. 2020, 142, 12288−12298